A High-Resolution Optical Transition Radiation Diagnostic for Fast-Electron Transport Studies

Introduction

High-current relativistic electron beams are generated by high-intensity laser interactions with solids.[1] These electron beams may have applications in compact, tabletop-based, high-brightness laser–plasma particle accelerators,[2] narrowband x-ray sources for medical applications,[3] x-ray sources for high-density inertial fusion energy (IFE) target backlighter radiography,[4] and collimated electron beams required for the fast-ignition approach to IFE.[5] The MeV fast electrons are generated in high-intensity laser–matter interactions, and their subsequent motion must be understood if their potential applications are to be fully realized. A promising technique that provides information about the fast-electron energy and divergence, as well as spatial and temporal distribution inside the target, is spatially resolving the spectrum of transition radiation (TR).[6] TR is emitted when a charged particle passes through a refractive index interface,[7] as in the case of fast electrons exiting a metal foil into vacuum. The emitted electromagnetic energy is undetectably small for a single electron; however, laser–solid interactions typically produce a large number of fast electrons whose individual contributions sum to provide a measurable signal. If the fast-electron beam possesses a strongly correlated longitudinal electron-density structure, the electromagnetic emission can undergo a considerable coherent enhancement, producing coherent transition radiation (CTR).[8] This enhancement is restricted to a narrow spectral band determined by the details of the longitudinal fast-electron density profile. Electrons accelerated by laser–matter interactions have the required longitudinal density profile to generate the CTR.[9] The exact form of this profile depends on the nature of the dominant acceleration mechanism. For example, the resonance absorption process[10] accelerates electrons into the target once per optical cycle, whereas the $\vec{v} \times \vec{B}$ component of the Lorentz force[11] accelerates electrons twice every optical cycle. These electrons then travel through the target as a train of microbunches separated in time by an optical period or half an optical period, generating a CTR signal at the fundamental or second harmonic of the laser frequency, respectively. The spatial-intensity distribution and spectrum of the CTR emission provide information about the electron-transport physics in solid density.[12]

Experimental Setup

A transition radiation diagnostic (TRD) has been designed to acquire high-resolution images of rear-side optical emission at the second harmonic ($\lambda \sim 527$ nm) of the laser frequency from laser-illuminated planar targets. In the optical design shown in Fig. 113.7, a 20× infinity corrected objective,[13] with a 20-mm working distance, a numerical aperture of 0.42, a 1.2-mm field of view, a 1.6-μm depth of focus, and a 0.7-μm resolving power, collects the optical emission from the target's rear surface. A 150-μm-thick sacrificial glass microscope cover slip, acting as a debris shield, is placed on the target side of the objective. The objective is mounted on a motorized 1-D linear actuator[14] with a 10-mm full range of motion and a 20-nm step size. The objective has an exit pupil diameter of 8.4 mm. A 4-mm-thick Schott KG5 glass filter with $\sim 10^{-10}$ transmission at $\lambda = 1053$ nm and $\sim 70\%$ transmission from $\lambda = 400$ to 600 nm prevents laser light from propagating through the system.[15] A 200-mm-focal-length achromatic lens focuses the light through a pinhole that blocks stray light. A narrowband 50/50 beam splitter steers the signal beam through 90°, and a unit magnification optical arrangement relays the light to the detector. A 24-nm bandpass filter centered on $\lambda = 529$ nm is placed in the collimated region of this path.[16] Optical-quality, neutral-density (ND) filters can be placed here to control the level of the signal without significantly compromising the spatial resolution. The overall transmission of the TRD at $\lambda = 527$ nm is $\sim 20\%$. The detector is a Spectral Instruments (SI) 800-series charge-coupled-device (CCD) camera with a dynamic range of 10^4 (Ref. 17). The 14-mm × 14-mm front-illuminated chip is composed of 1024 × 1024, 13.5-μm × 13.5-μm pixels with a full-well capacity of 10^5 electrons. At $\lambda = 527$ nm the CCD quantum efficiency is 20%. The CCD chip is cooled to –40°C to minimize dark current (<0.1 e–/pixel/s). The readout rate for the 16-bit analog-to-digital converter can be varied from 100 to 800 kHz, with a read noise of <5 electrons at the slowest speed.

To obtain high-resolution images of the target's rear-surface emission, the microscope objective must be positioned 20 mm away from the rear surface with ~ 1-μm precision. This is accomplished by using the second arm of the optical system
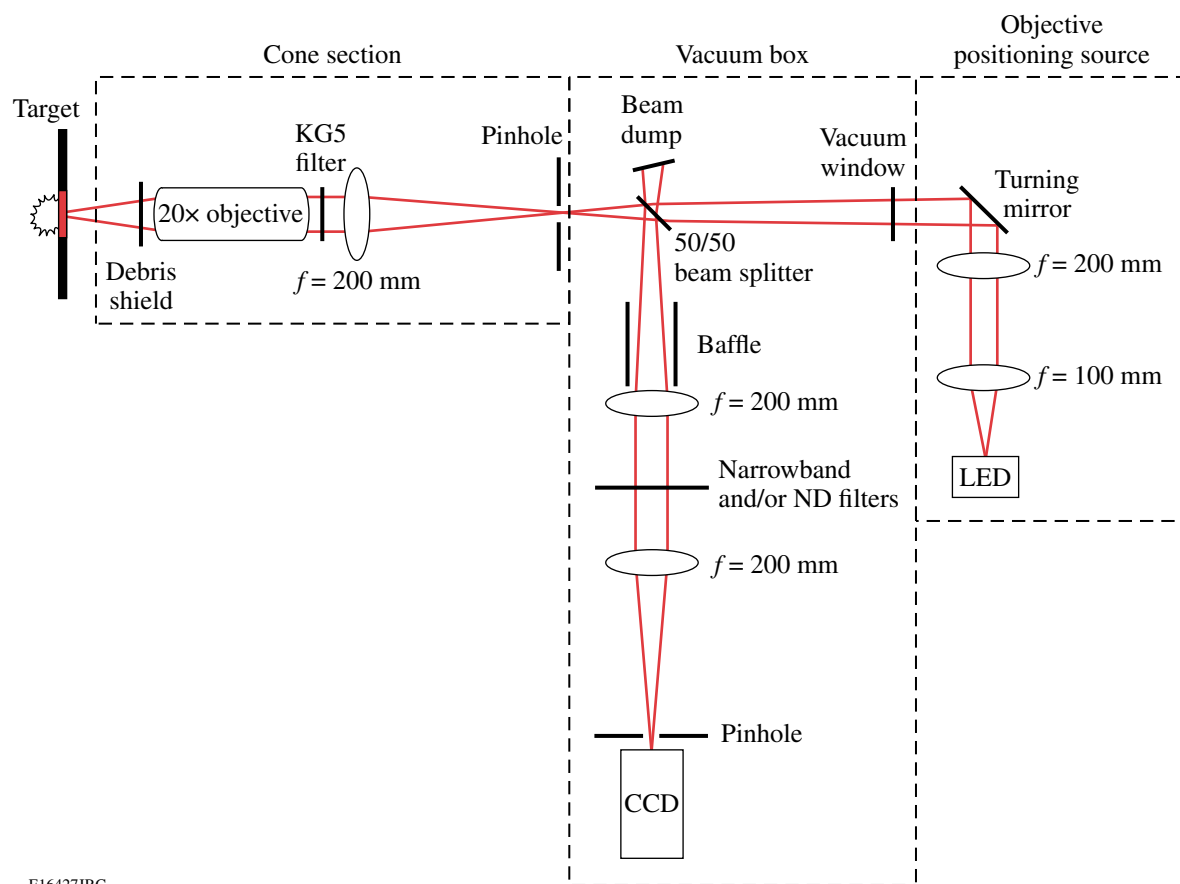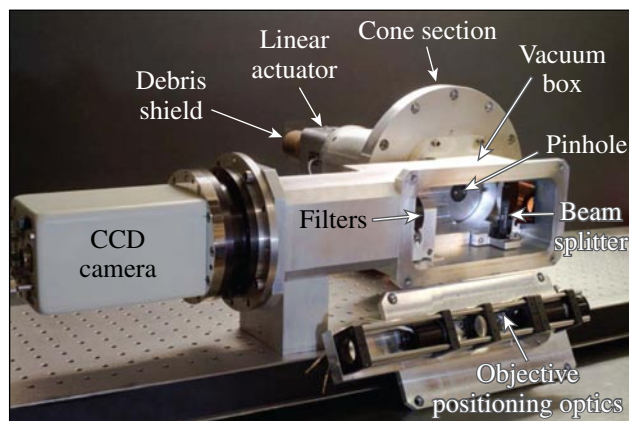
Figure 113.7
A schematic layout of the TRD optical system. Light emitted from the rear side of the target is magnified and relayed to a CCD camera. Filters and pinholes minimize background contributions. The right arm of the system is used only for pre-shot focusing on the rear surface.

(Fig. 113.7). Light from an ultrabright green LED[18] is transmitted through the collection optics and reflected off the target's rear side. Small-scale surface features present on the rear surface of the target act as focusing fiducials and are imaged onto the CCD camera. The camera's external shutter control channel is used to synchronize the LED illumination with the CCD chip exposure period. The CCD exposure time and readout speed are selected to accommodate the ND filter strength for the duration of this procedure. They are returned to standard values of 1 s and 400 kHz, respectively, for the experiment. The baffle and beam dump shown in Fig. 113.7 minimize the propagation of stray LED light through the system during positioning.

The TRD shown in Fig. 113.8 is comprised of two sections: The cone section resides inside the target chamber and is mounted on a target chamber port flange. The rear section, the TRD vacuum box, is attached to the outside face of the cone section. The rear panel of the vacuum box can be removed (as

Figure 113.8
A photograph of the TRD with the rear-side access panel removed and laid along side. A detailed discussion of the device is found in the text.

shown in Fig. 113.8) for easy access to the filtering optics and pinhole between shots. Vent holes in the KG5 filter mount link the TRD vacuum box volume to that of the target chamber, allowing the TRD to be pumped. This allows the CCD camera to be operated in vacuum without an independent vacuum system. Operating pressure is reached within 12 min. The TRD vacuum box can be isolated from the main volume of the target chamber by replacing the KG5 filter mount and allowing the KG5 filter to act as a vacuum window. A computer-controlled linear actuator provides high-precision positioning of the micro-scope objective (see Fig. 113.9). The objective is mounted to the carriage and driven by a pico-motor with a 20-nm step size over a 10-mm range. An encoder using a holographically ruled grating[19] provides closed-loop control of the objective position with ~0.5-μm precision. The system is enclosed in an aluminum casing. To mitigate the risks posed to the actuator circuitry by electromagnetic pulses, it is disconnected during the shot. The actuator maintains its position when powered down.
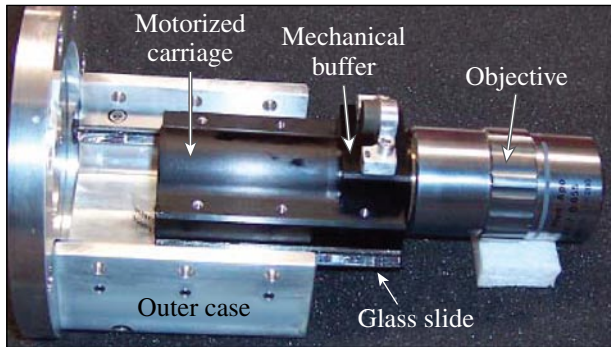
E16429JRC

Figure 113.9
The microscope objective is firmly held by the carriage, which glides in and out smoothly on rails attached to the inside of the outer case. The New Focus pico motor (not shown) is housed in the upper outer case and attached to the carriage via the mechanical buffer. It moves the objective in 20-nm steps over a range of 10 mm. Attached to the under side of the carriage is a glass slide encoded with a holographic ruler with 1-μm graduations. The hologram is read out from below by a reader embedded in the lower outer case to provide closed-loop positioning control.

The TRD was deployed on experiments conducted on LLE's Multi-Terawatt (MTW) Laser Facility.[20] This system is a front-end prototype for OMEGA EP.[21] The TRD is mounted on the MTW target chamber (shown in Fig. 113.10), where it occupies the port directly facing the off-axis parabolic focusing mirror. This assignment drove many components of the mechanical design. Significant amounts of γ radiation are produced in the forward direction during a high-intensity laser-target shot.[22] To prevent this radiation from contaminating the CTR signal, the system is folded through 90° so that the detector can be
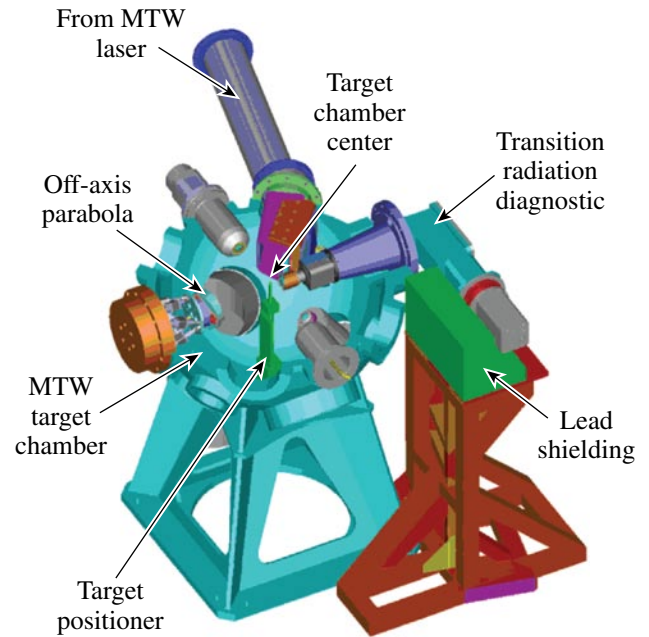
E16430JRC

Figure 113.10
A 3-D model of the MTW target chamber. An off-axis parabola (OAP) steers the MTW laser beam to focus at target chamber center (TCC). The TRD is housed in the port directly opposite the OAP. It images the rear-side optical emission from a normally illuminated target placed at TCC. The TRD optical system is folded through 90° so that the CCD camera lies in the γ-ray shadow of the TRD lead shielding.

shielded behind a 10-cm-thick lead brick wall. An additional 2-mm lead shield (not shown in Fig. 113.10) is placed around the CCD camera to minimize single hits by scattered γ rays arriving from the rear and top sides. Figure 113.11 illustrates the effect of the lead shielding in suppressing the number of γ-ray single hits. The images were taken under nearly identical experimental conditions. The solid-curve histogram was taken with no lead shielding in place. Individual γ rays are seen to produce pixel values of up to ~4000 analog-to-digital units. A reduction in the number of single hits by more than an order of magnitude was observed on the subsequent shot with the lead shielding in place (dashed-curve histogram).

System Performance

The calculated optical transmission curve for the TRD is shown in Fig. 113.12. The transmission of individual optical components was obtained either from the corresponding data sheet or by direct measurement using a spectrophotometer.[23] The curve shows that the transmission varies by 15 orders of magnitude between λ = 1053 nm and λ = 527 nm, so the laser light makes no contribution to an image obtained using the TRD. This was verified with 3-J laser shots taken on 20-μm-

thick, 500-μm-sq iron foils with the 24-nm bandpass filter replaced by an RG1000 filter glass.[15] This material efficiently transmits at the laser frequency while strongly attenuating its second harmonic. The results indicate that no light at the laser frequency enters the optical system.

The optical resolution of the TRD was determined by measuring the modulation transfer function (MTF).[24] The MTF of an imaging system is a measure of the image contrast at the object spatial frequencies; it describes with what efficiency
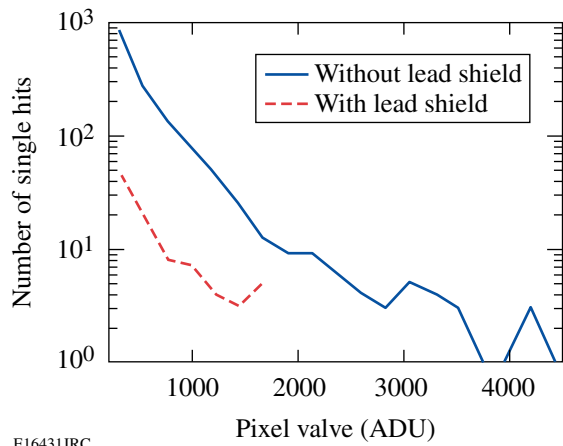
Figure 113.11
Histogram of the number of γ-ray single hits from two shots conducted under almost identical conditions. The pixel values are shown in analog-to-digital units (ADU's). The solid curve corresponds to a shot taken without lead shielding; the dashed curve corresponds to a shot with the lead shielding in place, demonstrating the efficiency of TRD shielding in suppressing the number of γ-ray photons incident on the CCD.
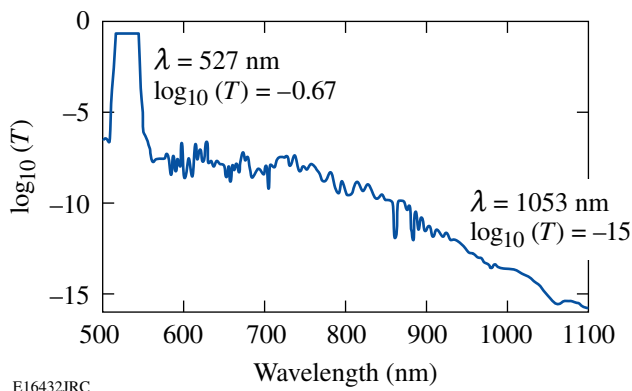
Figure 113.12
The optical transmission curve for the TRD. The transmission efficiency at the laser second harmonic, $\lambda = 527$ nm, is ~20%. The transmission efficiency at the laser wavelength, $\lambda = 1053$ nm, is ~15 orders of magnitude lower.

the system can pass each spatial frequency in the object plane. The optical resolution can be defined as the reciprocal of the highest frequency passed at which the contrast is maintained above a specified value. Tatian[25] has shown that the MTF can be obtained directly by analyzing equally spaced samples of the image edge function, which is the image space conjugate of a back-illuminated half plane as described below.

The experimental half plane was provided by an edge in a scanning electron microscope (SEM) 400-resolution grid [see Fig. 113.13(b)]. The grid was placed in the focal plane of the 20× objective, and an ultrabright LED illuminated the grid from its front side. The illumination was evenly distributed over the object plane to ensure good contrast in the object. The amount of stray light entering the optical system was minimized by mounting the SEM grid in a pinhole and constructing a set
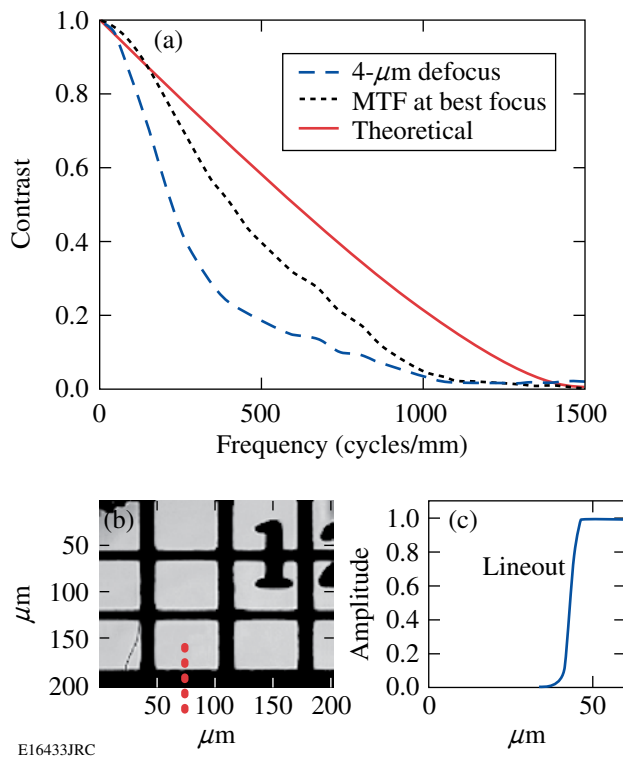
Figure 113.13
(a) The modulation transfer function (MTF) of the TRD. The curves are produced by analyzing images obtained using the TRD fitted with a 20× microscope objective. The solid line shows the theoretical MTF. The measured MTF at best focus is indicated by the dotted line; the contrast falls to ~1/10 at around 900 cycles/mm corresponding to a spatial resolution of ~1.1 μm. The dashed-line MTF expresses the effect of defocusing the collection optics. A 4-μm defocus reduces the optical performance of the system. (b) A section of an SEM 400-resolution grid. The dotted line indicates the position from which the lineout shown in (c) was taken. The lineout is normalized and used to calculate the MTF.

of opaque screens around the objective. The objective was positioned so that the grid was slightly defocused before being scanned through best focus. An image of the SEM grid was obtained every 500 nm, after which the images were post-processed to obtain the MTF. Figure 113.13(c) shows a normalized lineout, at best focus, taken through the image edge function. The CCD camera cannot sufficiently sample the image edge function with a 20× magnification, so it was necessary to linearly interpolate the data to effectively double the sampling rate to avoid aliasing in the MTF. Figure 113.13(a) shows the MTF for the case where a debris shield was placed in front of the objective. The solid line is the theoretical MTF; the dotted line shows the measured MTF at best focus. The limit of the spatial resolution is defined here to be the point at which the contrast ratio is ~10%. At best focus this corresponds to a spatial frequency of approximately 900 cycles/mm or 1.1 μm. Since it was necessary to linearly interpolate the image edge function, the value of 1.1 μm corresponds to the MTF of the optical part of the system. The CCD camera limits the optical resolution of the full system to ~1.4 μm, the size of a CCD pixel over the full field of view. This pixel-size–imposed limit could be reduced by increasing the system's magnification. The effect of defocus is illustrated in Fig. 113.13(a) by the dashed line MTF. A 4-μm defocus of the TRD collection optics reduces the MTF-limited resolution to about 1.5 μm at 10% contrast with the contrast falling about twice as fast as in the best-focus case.

The TRD has been fielded on experiments conducted to diagnose electron transport in a variety of solid materials of varying thickness under differing laser conditions. Figure 113.14 shows three characteristic images of the rear-side emission in both a linear (top) and a logarithmic (bottom) scale. From left to right the targets are 20-μm-thick aluminum, 30-μm-thick aluminum and 50-μm-thick copper; all are 500 μm in the transverse directions. These images are produced by light emitted at the target's rear surface in a narrow spectral window around $\lambda = 527$ nm, the laser second harmonic. The emission can be explained as CTR caused by a density-modulated relativistic electron beam generated by the $\vec{v} \times \vec{B}$ component of the Lorentz force. The upper-frame images clearly indicate the presence of small-scale structures, ~≥2 μm in the emission region, which is indicative of electron-beam filamentation.[26] The lower-frame images show that the filamentary structures are superimposed onto a ring-like structure. The annular pattern is almost always observed and suggests that only the electrons accelerated along the beam envelope possess the required density modulation to be observed with the CTR technique. Our calculations suggest that these electrons make up only a small fraction, <5%, of the total fast-electron population.
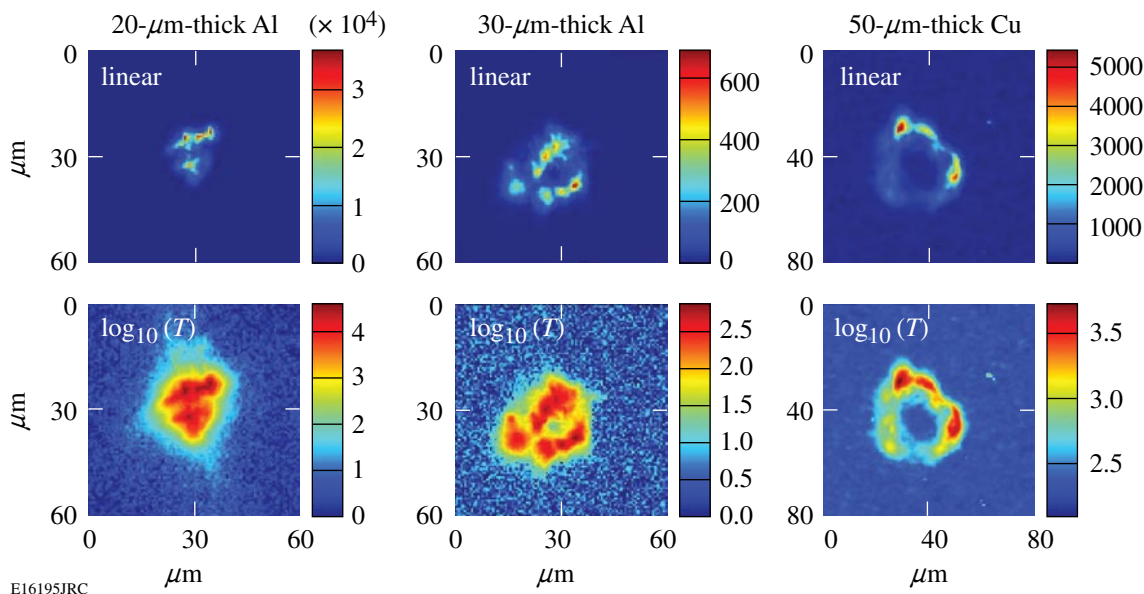

E16195JRC

Figure 113.14
Images of the rear-side optical emission from thin foil targets normally illuminated with a laser intensity of 10^{19} W/cm^2. The upper row shows the images plotted on a linear scale, while the lower row shows the corresponding log-scale representation. From left to right the images are from 20-μm-thick aluminum, 30-μm-thick aluminum, and 50-μm-thick copper. The upper-frame images indicate the presence of filamentary structures in the emission pattern. The lower images are demonstrating that the background emission pattern possesses an annular property.

Figure 113.14 further indicates that the spatial size of the emission region increases with target thickness. This is presented explicitly in Fig. 113.15, where the radius of the observed emission pattern is plotted against the target thickness. A least squares fit to the data shows that the beam diverges inside the target with a half angle of ~16°. The corresponding intercept with the radius axis indicates that the beam emerges from a source of radius ~4 μm, consistent with the spatial size of the focused MTW laser beam.

$$R = 0.28\,T + 4.34$$
$$\Rightarrow \theta_{1/2} \approx 15.7°\pm1°$$

Intercept = 4.34±0.95 ~ focal-spot radius
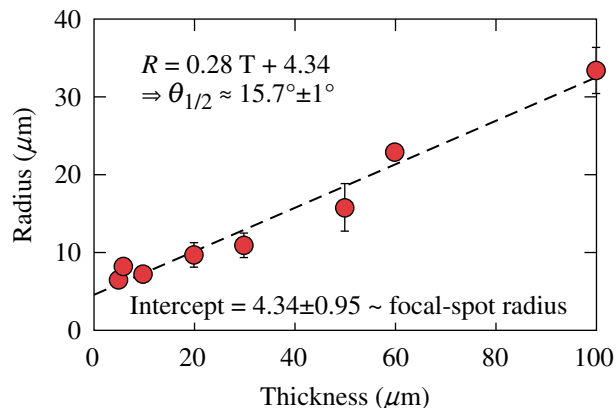
E16198JRC

Figure 113.15
The size of the rear-surface emission region grows with target thickness. The growth is consistent with a fast-electron divergence angle of 16°. The data has been fitted using a least squares routine. The intercept of the least squares fit with the radius axis, representing the size of the electron source, is ~4.5 μm and consistent with the size of the laser focus.

Summary

A coherent transition radiation diagnostic has been developed to image the rear-side emission from high-intensity-laser–irradiated foil targets. The device has been optimized to measure radiation in a 24-nm bandwidth around $\lambda = 529$ nm with a dynamic range of 10^4. The transmission at $\lambda = 527$ nm is 15 orders of magnitude higher than the transmission at the laser frequency, and no laser light has been detected in the system during experiments. We have demonstrated, by measuring the modulation transfer function, that the CCD pixel size limits spatial resolution to 1.4 μm. The diagnostic is being used to infer information about the transport of high-current relativistic electron beams through solid targets. Small-scale structures, ~2 μm in size, have been observed in the rear-surface emission of metal foils irradiated with laser intensities of ~10^{19} W/cm^2. These are indicative of electron-beam filamentation.

REFERENCES

1. M. H. Key, M. D. Cable, T. E. Cowan, K. G. Estabrook, B. A. Hammel, S. P. Hatchett, E. A. Henry, D. E. Hinkel, J. D. Kilkenny, J. A. Koch, W. L. Kruer, A. B. Langdon, B. F. Lasinski, R. W. Lee, B. J. MacGowan, A. MacKinnon, J. D. Moody, M. J. Moran, A. A. Offenberger, D. M. Pennington, M. D. Perry, T. J. Phillips, T. C. Sangster, M. S. Singh, M. A. Stoyer, M. Tabak, G. L. Tietbohl, M. Tsukamoto, K. Wharton, and S. C. Wilks, Phys. Plasmas **5**, 1966 (1998).

2. T. Katsouleas, Nature **444**, 688 (2006).

3. K. K. Kainz et al., Med. Phys. **31**, 2053 (2004).

4. H.-S. Park, D. M. Chambers, H.-K. Chung, R. J. Clarke, R. Eagleton, E. Giraldez, T. Goldsack, R. Heathcote, N. Izumi, M. H. Key, J. A. King, J. A. Koch, O. L. Landen, A. Nikroo, P. K. Patel, D. F. Price, B. A. Remington, H. F. Robey, R. A. Snavely, D. A. Steinman, R. B. Stephens, C. Stoeckl, M. Storm, M. Tabak, W. Theobald, R. P. J. Town, J. E. Wickersham, and B. B. Zhang, Phys. Plasmas **13**, 056309 (2006).

5. M. Tabak et al., Phys. Plasmas **1**, 1626 (1994).

6. S. D. Baton et al., Phys. Rev. Lett. **91**, 105001 (2003).

7. V. L. Ginzburg, Phys.-Usp. **39**, 973 (1996).

8. J. Zheng et al., Phys. Plasmas **10**, 2994 (2003).

9. J. C. Adam, A. Héron, and G. Laval, Phys. Rev. Lett. **97**, 205006 (2006).

10. W. L. Kruer, *The Physics of Laser Plasma Interactions*, Frontiers in Physics (Westview Press, Boulder, CO, 2003), pp. 39–43.

11. S. C. Wilks et al., Phys. Rev. Lett. **69**, 1383 (1992).

12. H. Popescu et al., Phys. Plasmas **12**, 063106 (2005).

13. M-plan Apo 20×, Mitutoyo, Japan.

14. New Focus, Inc., a division of Brookham, San Jose, CA, 2004, http://www.newfocus.com (14 December 2004).

15. Schott North America, Inc., Elmsford, NY 10523.

16. Semrock, Rochester, NY 14624.

17. Spectral Instruments, Tucson, AZ 85745 (http://www.specinst.com/files/datasheets/4204-.pdf).

18. Luxeon III Star, Philips Lumileds Lighting Company, San Jose, CA 95131.

19. LIP 481R, Heidenhain, 83301 Traunreut, Germany.

20. V. Bagnoud, in *Frontiers in Optics 2004* (Optical Society of America, Rochester, NY, 2004), Paper FMM2.

21. J. H. Kelly, L. J. Waxer, V. Bagnoud, I. A. Begishev, J. Bromage, B. E. Kruschwitz, T. J. Kessler, S. J. Loucks, D. N. Maywar, R. L. McCrory, D. D. Meyerhofer, S. F. B. Morse, J. B. Oliver, A. L. Rigatti, A. W. Schmid, C. Stoeckl, S. Dalton, L. Folnsbee, M. J. Guardalben, R. Jungquist, J. Puth, M. J. Shoup III, D. Weiner, and J. D. Zuegel, J. Phys. IV France **133**, 75 (2006).

22. S. P. Hatchett, C. G. Brown, T. E. Cowan, E. A. Henry, J. S. Johnson, M. H. Key, J. A. Koch, A. B. Langdon, B. F. Lasinski, R. W. Lee, A. J. MacKinnon, D. M. Pennington, M. D. Perry, T. W. Phillips, M. Roth, T. C. Sangster, M. S. Singh, R. A. Snavely, M. A. Stoyer, S. C. Wilks, and K. Yasuike, Phys. Plasmas **7**, 2076 (2000).

23. Lambda900 Spectrophotometer, PerkinElmer, Waltham, MA 02451.

24. J. W. Goodman, *Introduction to Fourier Optics*, 3rd ed. (Roberts and Company Publishers, Englewood, CO, 2005), Chap. 6, p. 127.

25. B. Tatian, J. Opt. Soc. Am. **55**, 1014 (1965).

26. L. Gremillet, G. Bonnaud, and F. Amiranoff, Phys. Plasmas **9**, 941 (2002).